Article

Wafer-Scale Si-Based Metal−Insulator−Semiconductor Photoanodes for Water Oxidation Fabricated Using Thin Film Reactions and Multiple-layer Electrodeposited Catalysts

Soonil Lee,[†] Shang-Hsuan Wu,[†] and Edward T. Yu*

Cite This: https://doi.org/10.1021/acsaem.4c00016

Read Online

ACCESS | Metrics & More | Article Recommendations | Supporting Information

ABSTRACT: Solar-driven photoelectrochemical (PEC) water splitting offers a promising and environmentally friendly route for the conversion of renewable solar energy to hydrogen gas. A crystalline Si absorber is especially attractive due to its moderate bandgap, high charge mobility, long carrier diffusion length, cost-effectiveness, and scalability in manufacturing. To improve the stability of Si-based PEC cells in operation, metal−insulator−semiconductor (MIS) structures have been widely employed. In this work, we employ simple and highly scalable processes to fabricate high-performance, extremely stable Si-based MIS photoanodes, and demonstrate their application to the fabrication of wafer-scale photoanodes. Localized conduction paths formed via an Al/SiO$_2$ thin-film reaction enable low-resistance charge extraction even through thick insulating layers, yielding photoanodes with excellent stability. To improve the efficiency, we demonstrate a two-step Ni/NiFe electrodeposition process to create efficient oxygen evolution reaction catalysts. The Ni/NiFe catalyst allows for a high Schottky barrier between Si and Ni, lowering the photoanode onset potential, while the NiFe surface layer improves the catalytic performance. An unassisted solar-driven water splitting system incorporating a wafer-scale photoanode and monocrystalline Si solar cells is demonstrated and yields a solar-to-hydrogen conversion efficiency of 6.9% under simulated AM 1.5G sunlight illumination.

KEYWORDS: solar water splitting, photoelectrode, photoanode, thin-film reaction, electrodeposition, metal−insulator−semiconductor structure, NiFe catalyst, solar energy
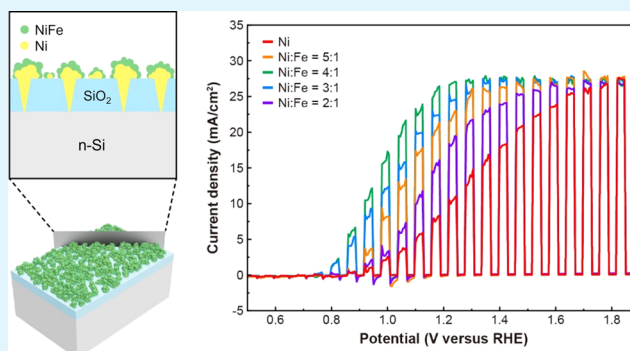
INTRODUCTION

Green production of hydrogen (H$_2$) is expected to play a key role in the transition from fossil-dominated energy sources to cleaner and more sustainable energy systems. Solar-driven photoelectrochemical (PEC) water splitting enables the direct generation of H$_2$ gas from water using solar illumination. In PEC cells, semiconductor materials are used for absorbing photons under solar illumination to generate electron−hole pairs for H$_2$ and/or oxygen (O$_2$) evolution.[1−4] Crystalline Si is an especially attractive semiconductor absorber material for photoelectrodes in PEC cells since it is abundant, has a moderate bandgap (1.12 eV) and high carrier mobility,[5] and due to the large existing technology base for Si photovoltaics (PV) is highly cost-effective to manufacture at scale. However, Si-based photoanodes remain scientifically and technologically challenging, since the oxygen evolution reaction (OER) requires a complex four-electron process and Si has poor stability in alkaline solutions. To address the stability issue, metal−insulator−semiconductor (MIS) structures with insulating oxide protective layers have been widely used for Si-based photoanodes.[6−16] Catalysts, which improve OER kinetics and enhance PEC cell efficiency, include Fe,[17,18] Ni,[7,11,19] RuO$_X$,[8,20−23] IrO$_X$,[24−26] NiFe,[6,10,16,27] and NiCo.[28−30]

In MIS photoelectrodes, photogenerated charges are typically extracted from the semiconductor to the metal catalyst via tunneling through the insulator. The insulator thickness plays a key role in such MIS photoelectrodes since it influences both efficiency and long-term stability. Tunneling of photogenerated charges decreases exponentially with increasing insulator thickness so that an insulator with thickness under ∼5 nm is required for high efficiency.[31,32] Conversely, a thicker insulator is beneficial for protecting the semiconductor surface from chemical corrosion, with a minimum insulator thickness of 50 nm having been cited as a requirement for long-term stability.[33,34] To overcome this trade-off between
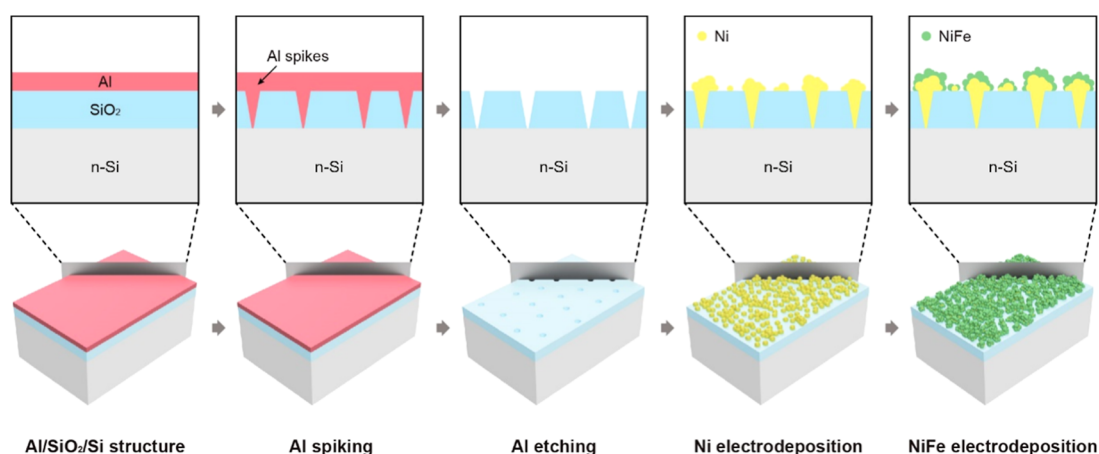
Figure 1. Key fabrication steps. Schematic illustrations are shown of the key steps in fabrication of the spiked NiFe/Ni/SiO$_2$/Si MIS photoanode structures.
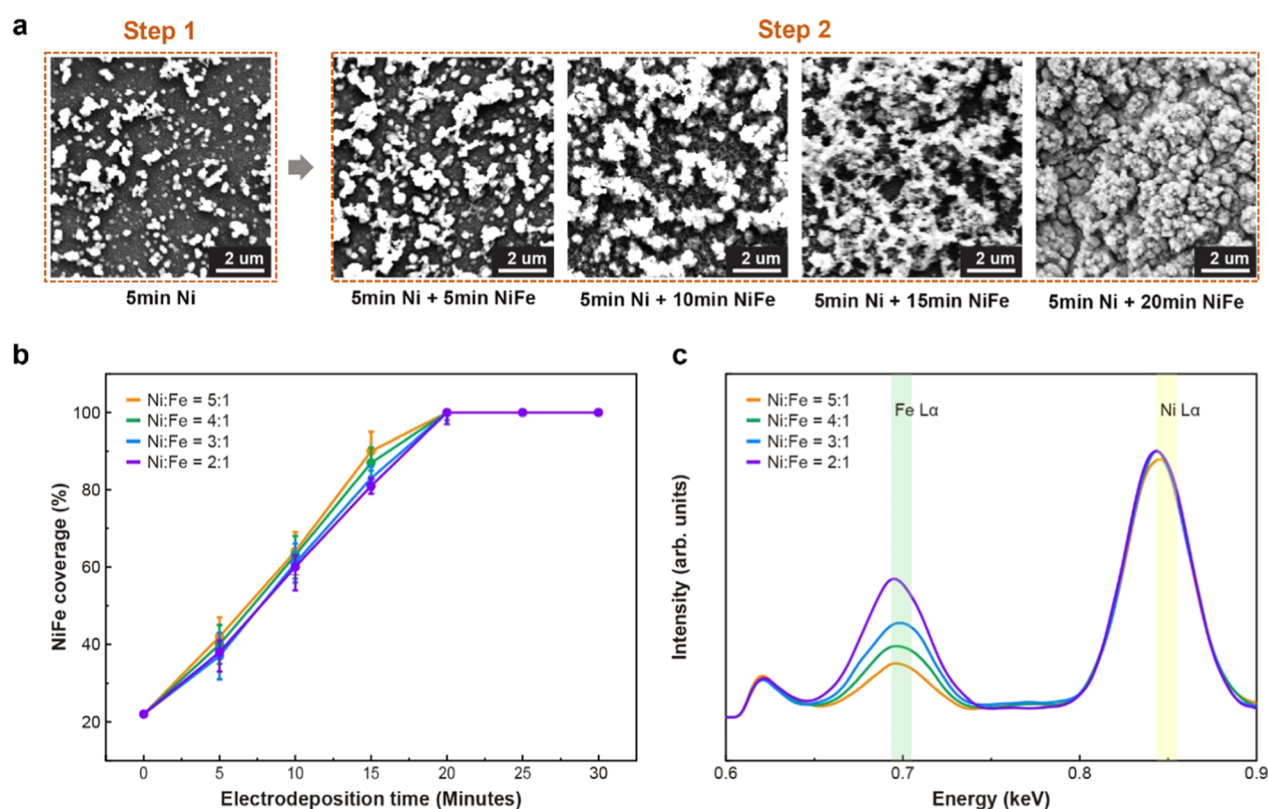

Figure 2. Characterization of double-layered NiFe/Ni electrodeposition. (a) Plan-view SEM images of the spiked Ni/SiO$_2$/Si (step 1) and spiked NiFe/Ni/SiO$_2$/Si (step 2) surfaces created by electrodeposition with an applied bias of −3.0 V and different sequential electrodeposition times. (b) NiFe coverage on the spiked Ni/SiO$_2$/Si surface as a function of electrodeposition time. (c) EDX spectra of the spiked Ni/SiO$_2$/Si surface with different amounts of FeSO$_4$ (0.004, 0.005, 0.007, and 0.01 M) in NiFe plating solutions used for electrodeposition. The Ni/Fe ratios shown are those determined by the peak intensity between Ni Lα peak and Fe Lα peak from EDX spectra.

efficiency and stability, our previous work on Si-based MIS photoanodes used an Al thin-film reaction with SiO$_2$ to generate localized Al "spikes" which penetrate through the thick SiO$_2$ thick layer. These were then replaced by a Ni catalyst via etching and electrodeposition to create local conductive paths through the thick SiO$_2$ layer for photo-generated minority charge transport.[7] The thick SiO$_2$ layer (90 nm) yielded excellent long-term stability for the Si-based MIS photoanode in an alkaline solution. However, the applied bias photon-to-current efficiency (ABPE) was still relatively modest, most likely limited by the catalyst material. A recent

study has reported the use of NiFe catalysts for a Si-based MIS photoanode, with the incorporation of Fe into Ni yielding a lower OER overpotential, making the NiFe alloy a highly efficient OER catalyst.[27]

Herein, we demonstrate wafer-scale Si-based MIS photo-anodes using the Al−SiO$_2$ thin-film reaction approach from our previous work[7] combined with electrodeposition of NiFe/Ni double-layered catalyst. The NiFe/Ni double-layered catalyst was deposited via a two-step electrodeposition process and yielded dramatic improvements in the OER activity compared to pure Ni catalyst. The Ni/Si interface has a higher

Schottky barrier compared to the NiFe/Si interface so that the NiFe/Ni double-layered catalyst leads to higher local hole concentration at the Si surface and consequently a reduced onset potential, while the NiFe at the surface yields improved catalytic performance. The thermally grown 90 nm SiO$_2$ layer provides antireflection functionality as well as long-term stability of the Si-based MIS photoanode. The resulting spiked NiFe/Ni/SiO$_2$/Si photoanode shows highly improved ABPE compared to that achieved with a pure Ni catalyst. To demonstrate the feasibility of this fabrication approach for the scalable unassisted water splitting system, we fabricate a wafer-scale photoanode and combine it with crystalline Si PV cells[35] to form a PEC/PV configuration which exhibits solar-to-hydrogen (STH) conversion efficiency of 6.9% under simulated AM 1.5G sunlight illumination.

■ RESULTS AND DISCUSSION

MIS Photoanode Fabrication. The fabrication process for a scalable Si-based MIS photoanode using the Al thin-film reaction and two-step NiFe/Ni electrodeposition is summarized in Figure 1. A dense and uniform SiO$_2$ insulating layer was grown on the n-Si substrate by using dry thermal oxidation. The SiO$_2$ layer thickness was designed to be 90 nm to minimize surface reflections in water in the 400−900 nm wavelength range. 90 nm of SiO$_2$ layer is expected to be sufficiently thick to protect the Si surface in alkaline solution since it has been reported that an insulator layer thickness over 50 nm is sufficient for good long-term stability.[34] For the formation of localized conducting paths through the SiO$_2$ layer, 100 nm Al was deposited on the SiO$_2$/n-Si substrate by DC sputtering and the Al/SiO$_2$/Si substrate was annealed under vacuum at 550 °C for 24 h, leading to localized Al spikes that penetrated completely through the 90 nm SiO$_2$ layer and contacted the Si substrate. The Al spikes were randomly distributed across the Al/SiO$_2$/Si substrate with an average density of 1.2×10^8 cm^{-2}. Following the thin-film reaction, the substrate was diced into chips for the fabrication of small-area (100 mm^2) photoanodes. The Al layer was then removed by chemical etching, and Ni and NiFe catalysts were sequentially deposited on the spiked SiO$_2$/Si substrate by electrodeposition. It has been reported that NiFe performs better as a catalyst for OER than Ni.[27] However, the NiFe/Si interface has a lower Schottky barrier compared with the Ni/Si interface. The NiFe/Ni/Si structure created by the two-step electrodeposition process described in detail below provides the increased Schottky barrier height associated with the Ni/Si interface combined with the superior catalytic activity of NiFe. Since both the Al thin-film reaction and electrodeposition processes are readily adaptable for wafer-scale fabrication, a full wafer-scale spiked NiFe/Ni/SiO$_2$/Si photoanode was also fabricated, with the entire process performed on a 4-in. Si wafer.

Electrodeposition of Double-Layered NiFe/Ni Catalyst. NiFe/Ni double-layered catalyst structures were created by a two-step electrodeposition process using a different plating solution for each material, starting with Ni. During Ni electrodeposition, Ni initially fills the Si exposed area on the spiked SiO$_2$/Si substrate due to the higher electric fields between the solution and Si layer and the very low electrical conductivity of SiO$_2$, resulting in the formation of an array of localized Ni/Si Schottky contacts. Subsequently, Ni nanoislands form from the initial Ni/Si contact regions. Ni electrodeposition was performed until the voids in the SiO$_2$

layer were entirely covered, leaving no exposed Si areas. Figure 2a shows scanning electron microscopy (SEM) images of NiFe electrodeposited on the spiked Ni/SiO$_2$/Si substrate with increasing deposition time. The surface coverage of electrodeposited NiFe/Ni catalyst layers was determined based on SEM images. These Ni nanoislands cover the voids with ∼22% total surface coverage on the SiO$_2$/Si substrate (step 1). Following the formation of Ni nanoislands on the spiked SiO$_2$/Si substrate, NiFe electrodeposition was performed (step 2). To optimize the NiFe/Ni catalyst structures, the morphology and element ratio between Ni and Fe (Ni/Fe ratio) of NiFe was controlled by varying the deposition time and the ratio between NiSO$_4$ and FeSO$_4$ in the NiFe plating solution for electrodeposition. Table 1 shows the detailed composition of

Table 1. Composition of NiFe Plating Aqueous Solutions Used for Electrodeposition

Ni/Fe ratio	NiSO$_4$ (M)	FeSO$_4$ (M)	H$_3$BO$_4$ (M)	L-histidine	H$_2$O (mL)
5:1	0.05	0.01	0.04	0.05	30
4:1	0.05	0.007	0.04	0.05	30
3:1	0.05	0.005	0.04	0.05	30
2:1	0.05	0.004	0.04	0.05	30

prepared NiFe plating solutions with different concentrations of NiSO$_4$ and FeSO$_4$ for corresponding Ni/Fe ratios (5:1 to 2:1). The deposition time has a significant effect on the surface coverage of NiFe/Ni, with the thicknesses and lateral extent of the NiFe/Ni nanoislands increasing gradually with an increase in the deposition time. NiFe/Ni nanoislands eventually coalesce on the SiO$_2$ surface after 20 min of NiFe deposition. Figure 2b shows the NiFe/Ni coverage on the SiO$_2$ layer as a function of the electrodeposition time using different NiFe plating solutions. The NiFe/Ni coverage steadily increases and reaches 100% after 20 min of NiFe deposition. This trend between NiFe/Ni coverage and deposition time was similarly observed for all electrodeposition processes with different NiFe plating solutions. The Ni/Fe ratios of deposited NiFe islands were analyzed by energy-dispersive X-ray spectroscopy (EDX) measurements on the surface. The peak intensity of Ni and Fe Lα peaks are normalized based on the reference Si Kα peak. Figure 2c shows the EDX spectra of spiked NiFe/Ni/SiO$_2$/Si surfaces formed by 30 min of electrodeposition using different NiFe plating solutions. A decrease in the Fe Lα peak is observed for the spiked NiFe/Ni/SiO$_2$/Si substrate when the amount of FeSO$_4$ is reduced in the NiFe plating solution for electrodeposition. This result indicates that the Ni/Fe ratio can be controlled from 5:1 to 2:1 by varying the ratio between NiSO$_4$ and FeSO$_4$ in NiFe plating solution from 0.004 to 0.01 M.

Numerical Analysis of Photoanode Potential Distributions. Use of the double-layer NiFe/Ni catalyst is essential in optimizing the photoanode performance. The metal catalyst plays a key role in improving the efficiency of photoanodes by enhancing the overall reaction rate, minimizing overpotential, and enhancing charge transport at the interface with the electrolyte. Ni is known as a good OER catalyst for Si-based MIS photoanodes, and its catalytic effect can be greatly enhanced by adding Fe impurities.[36] It has been reported that a photoanode with a NiFe catalyst shows better efficiency compared to that with a Ni catalyst.[37] However, in our device structure, the metal catalysts make direct contact with Si to
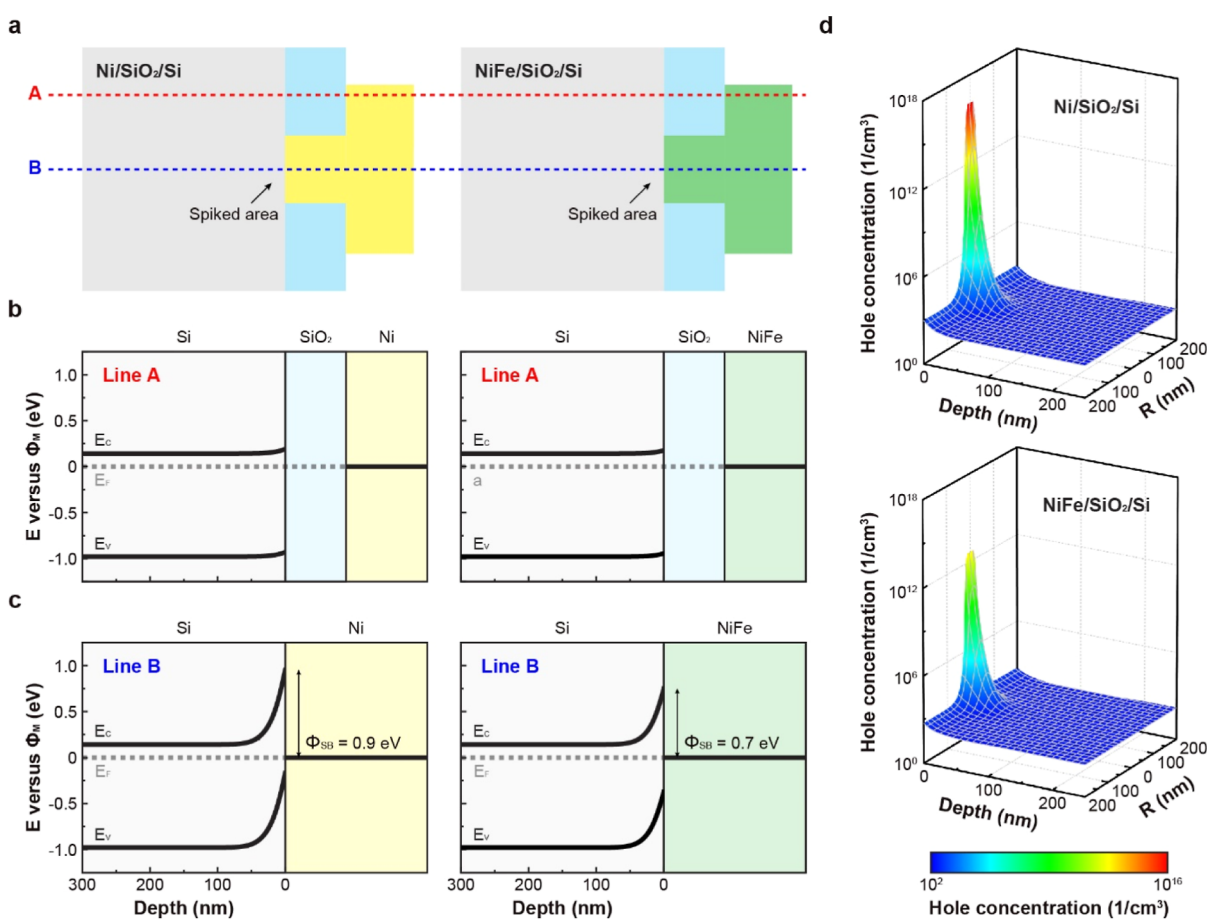
Figure 3. Simulations showing potential distributions for different models. (a) Schematic illustration of simulated model structures for MIS photoanodes: Ni/SiO$_2$/Si (model 1) and NiFe/SiO$_2$/Si (model 2) with 90 nm SiO$_2$ thickness and center spikes. (b,c) Simulated band diagrams at the interface area along the lines labeled in part (a) as A (b) and B (c) for Ni/SiO$_2$/Si and NiFe/SiO$_2$/Si. (d) Simulated hole concentration near the spiked area for Ni/SiO$_2$/Si and NiFe/SiO$_2$/Si structures.

form a Schottky barrier. Because of the lower work function of Fe compared to that of Ni,[38] the NiFe/Si interface forms a lower Schottky barrier compared to the Ni/Si interface,[39] causing lower hole accumulation at the Si surface. The effects of Schottky contacts between the metal catalyst and Si at the spiked area were analyzed computationally by using a commercial numerical finite-element solver, COMSOL Multiphysics. As shown in Figure 3a, two different model structures were simulated to assess the effect of different metal contact materials. The structures consist of metal/SiO$_2$/Si with a metal spike at the center and a 90 nm SiO$_2$ thickness. The metal spike has a diameter of 60 nm and contacts the Si at the bottom with an ideal Schottky contact. Ni and NiFe were set as the metal materials for model 1 and 2, respectively. The electric potential, field, and charge concentration were simulated for band structures of model 1 and 2.

Figure 3b shows the simulated band structures and hole concentrations of models 1 and 2. The electrical behaviors were analyzed for two different types of interfaces along the lines labeled A and B, the interfaces for which consist of metal/SiO$_2$/Si and metal/Si contacts, respectively, representing nonspiked and spiked regions. Previous reports have proven the utility of modeling Schottky barrier height for improving photovoltage in photoanodes by MIS capacitor model.[9,40,41] Herein, Ni has a higher work function (5.0 eV)[41] than the NiFe alloy (4.8 eV),[37] leading to stronger surface inversion at

the metal/Si interface (line B) in model 1 compared to model 2. However, due to the thick SiO$_2$ layer (90 nm), the difference is suppressed at the metal/SiO$_2$/Si interface (line A) and similarly weak band bending is observed along line A in both models. Therefore, similarly low concentrations of holes ($\sim$10^3/cm^3) are accumulated at the Si surface of the nonspiked areas. In the ideal Schottky contact model, direct contacts between Si and Ni and NiFe are formed with Schottky barriers (Φ_{SB}) of 0.9 and 0.7 eV at the spiked area, respectively. In the simulation, Schottky barriers were for simplicity determined by the full difference in work functions between Ni and NiFe. The actual barrier heights may be less than those in the simulations due to Fermi level pinning at the metal/Si interface.[42] Since the electrodeposition was performed at room temperature, Ni-silicide or Fe-silicide is unlikely to be formed at the Ni/Si and NiFe/Si interfaces.[43,44] As shown in Figure 3c, the larger Schottky barrier between Si and Ni in model 1 causes stronger surface inversion at the Si surface compared to that in model 2. The hole concentrations at the interfaces of Ni/SiO$_2$/Si and NiFe/SiO$_2$/Si were simulated as a function of the radial distance R from the center of the spiked area and depth from Si surface as shown in Figure 3d. The hole concentration at the Si surface increases toward the center of the spiked area for both model 1 and 2. Due to the higher Schottky barrier, higher hole concentrations are present at the Ni/Si interface compared to the NiFe/Si interface near the spiked area. While not intended
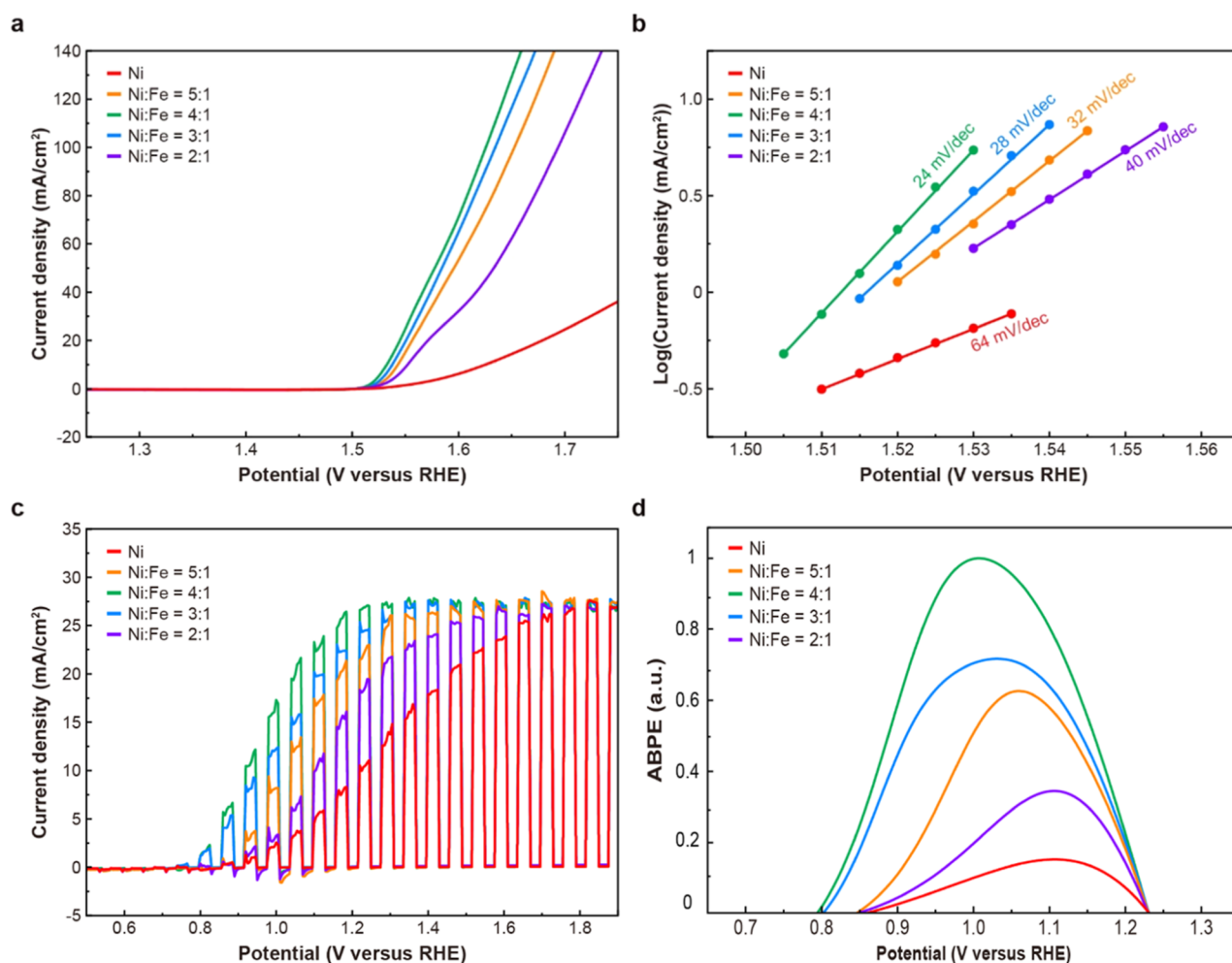
Figure 4. PEC characterization of photoanodes for different Ni/Fe ratios. (a) OER polarization curves and (b) Tafel plots for electrodeposited NiFe films on Ni plates in 1 M KOH solution with different Ni/Fe ratios in NiFe alloys (Ni/Fe = 5:1, 4:1, 3:1, and 2:1). (c) LSV curves and (d) normalized ABPE curves for spiked NiFe/Ni/SiO$_2$/Si photoanodes with different Ni/Fe ratios in the NiFe catalyst layers (Ni/Fe = 5:1, 4:1, 3:1, and 2:1).

to be quantitatively predictive, this result indicates that the localized spikes in the MIS photoanode should enable improvement in photovoltage, and the Ni/Si interface also leads to improved photovoltage due to its higher Schottky barrier compared with the NiFe/Si interface. Therefore, an improvement in onset potential can be expected by using NiFe/Ni double-layered catalyst for the spiked NiFe/Ni/SiO$_2$/Si photoanode.

PEC Performance of NiFe/Ni/SiO$_2$/Si Photoanodes. For NiFe alloy catalysts, it has been reported that the OER catalytic effect varies with the ratio of Ni to Fe.[27] To determine the optimum Ni/Fe ratio for the OER catalyst, LSV polarization curves were recorded under the water electrolysis setting in which the ~5 μm thick NiFe films with different Ni/Fe ratios (5:1 to 2:1) were electrodeposited on Ni plates. The planar feature of the NiFe film was observed in the plan-view SEM image (see Figure S1 in the Supporting Information). As shown in Figure 4a, enhanced OER activities with an onset at 1.5 V versus RHE were observed for all NiFe alloys compared to Ni (1.58 V versus RHE). As Fe content in the NiFe alloys is increased, the catalytic effect of the NiFe improves until a composition of Ni/Fe = 4:1 is reached. The improved onset potential in NiFe alloys can be ascribed to the introduction of Fe impurity in Ni catalyst that promotes the electrocatalytic

water oxidation reactions.[36,45] However, after that optimal point, additional Fe incorporation leads to degradation of the catalytic effect of NiFe. Figure 4b shows the Tafel slopes for Ni and NiFe alloys deduced from the OER polarization curves in Figure 4a. For the NiFe alloy with Ni/Fe = 4:1, the Tafel slope is 24 mV/dec which is the lowest compared to Ni and NiFe catalysts with other Ni/Fe ratios, indicating that the Ni/Fe = 4:1 composition is optimal for efficient charge transfer between the metal catalyst and electrolyte in an alkaline solution. PEC performance was measured for spiked NiFe/Ni/SiO$_2$/Si photoanodes in a 1 M KOH aqueous solution with a standard three-electrode system under illumination from an unfiltered 150 W xenon lamp. To further investigate the OER performance of NiFe and Ni for Si photoanodes, LSV measurements with chopped illumination were carried out for spiked NiFe/Ni/SiO$_2$/Si photoanodes with different Ni/Fe (see Figure 4c). The NiFe layers were electrodeposited on the Si photoanodes with constant NiFe/Ni coverage (~60%) and the Ni/Fe ratio of the NiFe layer varied from 5:1 to 2:1. All spiked NiFe/Ni/SiO$_2$/Si photoanodes show highly enhanced OER activity (0.8 V versus RHE) compared to that of Ni/SiO$_2$/Si photoanodes (0.92 V versus RHE), indicating improved catalytic activity for the NiFe catalyst compared to Ni. The spiked NiFe/Ni/SiO$_2$/Si photoanode with Ni/Fe =
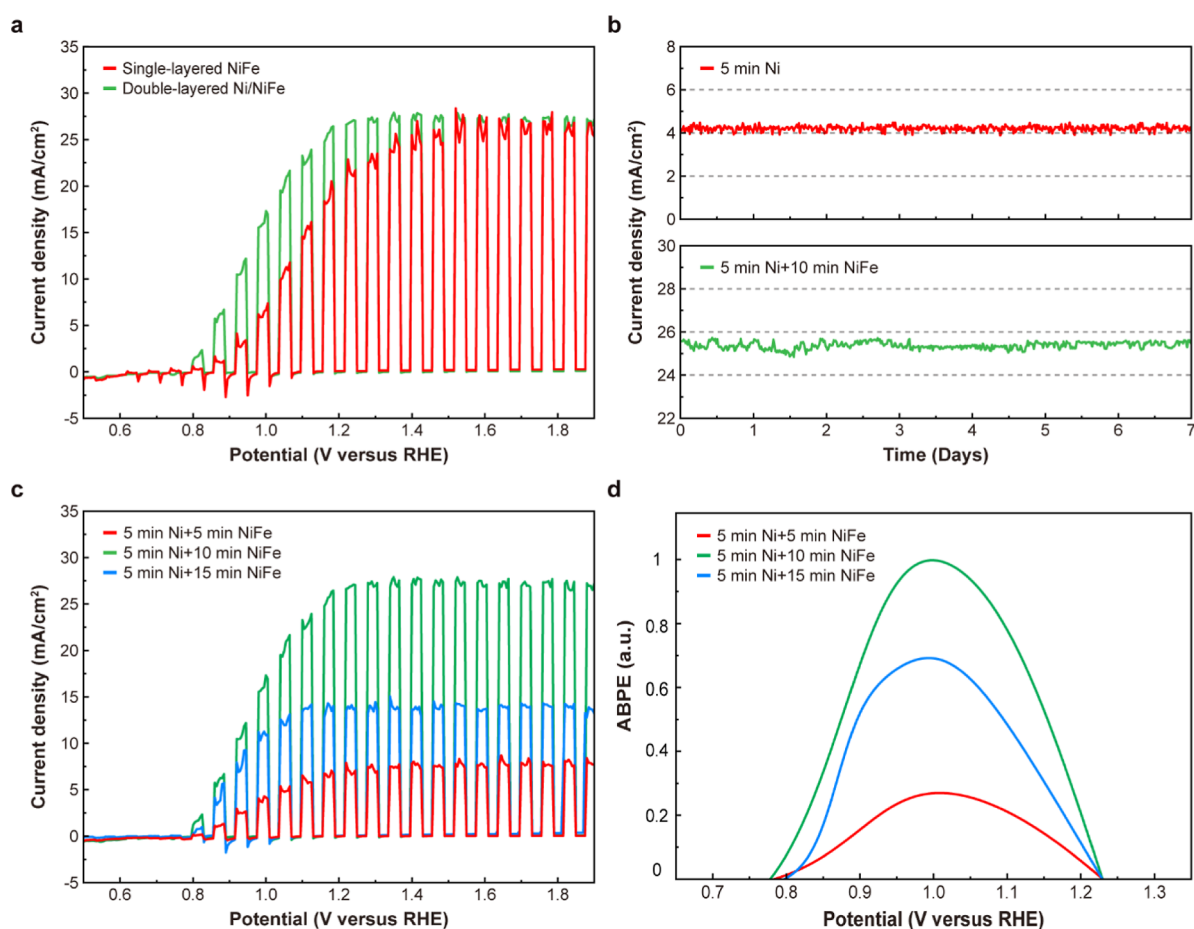
Figure 5. PEC characterization of photoanodes for different NiFe/Ni coverages. (a) LSV curves with chopped illumination in 1 M KOH solutions for the spiked single-layered NiFe/SiO$_2$/Si and spiked double-layered NiFe/Ni/SiO$_2$/Si photoanodes (Ni/Fe = 4:1). (b) 7 day CA stability tests at 1.23 V versus RHE in 1 M KOH solutions for spiked Ni/SiO$_2$/Si and NiFe/Ni/SiO$_2$/Si photoanodes with 5 min Ni electrodeposition and 5 min Ni + 10 min NiFe electrodeposition, respectively. (c) LSV curves and (d) normalized ABPE curves for spiked NiFe/Ni/SiO$_2$/Si photoanodes with NiFe electrodeposition times of 5, 10, and 15 min.

4:1 shows the best OER activity. As shown in Figure 4d, the normalized ABPE curves with different Ni/Fe ratios in the NiFe layer were used to compare the OER performance under different applied biases. The results confirm that the NiFe catalyst with Ni/Fe = 4:1 shows improved charge transfer properties and leads to the best photoanode OER performance. Similar differences in the onset potential of Ni and NiFe have been observed previously.[16]

Figure 5a shows the PEC performance for spiked MIS photoanodes fabricated with either pure NiFe or NiFe/Ni catalyst layers. Spiked MIS photoanode structures were prepared by electrodeposition of either single NiFe or double-layered NiFe/Ni catalyst layers on the spiked SiO$_2$/Si substrates. Both catalyst layers were deposited with the same surface coverage and Ni/Fe = 4:1 on the surface. As shown in Figure 5a, the spiked single-layered NiFe/SiO$_2$/Si photoanode shows clear OER activity with an onset potential of 0.85 V versus RHE and saturation current density of 25 mA/cm^2 due to the catalytic effect of the NiFe catalyst. A clear improvement in OER performance was observed with the double-layered NiFe/Ni catalyst, which shows a lower onset potential (0.80 V versus RHE). This result demonstrates that the double-layered NiFe/Ni catalyst improves the onset potential for the OER, which based on the numerical simulations shown in Figure 3 we attribute to the higher Schottky barrier for the Ni/Si

compared to the NiFe/Si and the resulting higher hole concentration at the Si surface for the former. At the same time, the thick SiO$_2$ layer (90 nm) provides good corrosion resistance for the spiked NiFe/Ni/SiO$_2$/Si photoanodes in an alkaline solution, even with high pH. Figure 5b shows 7 days of chronoamperometry (CA) stability tests for a Ni/SiO$_2$/Si photoanode and a NiFe/Ni/SiO$_2$/Si photoanode. Notably, during the stability tests, more fluctuation in photocurrent density in the NiFe/Ni/SiO$_2$/Si photoanode was observed, which can be ascribed to the higher OER activity that caused more O$_2$ bubbles generated on the surface and suppressed the OER until detaching. As shown in Figure 5b, the spiked Ni/SiO$_2$/Si photoanode shows excellent stability with no degradation after 7 days of continuous operation. The spiked NiFe/Ni/SiO$_2$/Si photoanode also shows high corrosion resistance with no decline in the photocurrent during the 7 day stability test. This result confirms that the NiFe/Ni double-layered catalyst with a spike structure through the thick SiO$_2$ layer maintains its OER catalytic effect without degradation in alkaline solution. The much higher, sustained photocurrent density in the spiked NiFe/Ni/SiO$_2$/Si photoanode confirms that the NiFe/Ni double-layered catalyst improves its OER catalytic effect without degradation in alkaline solution.
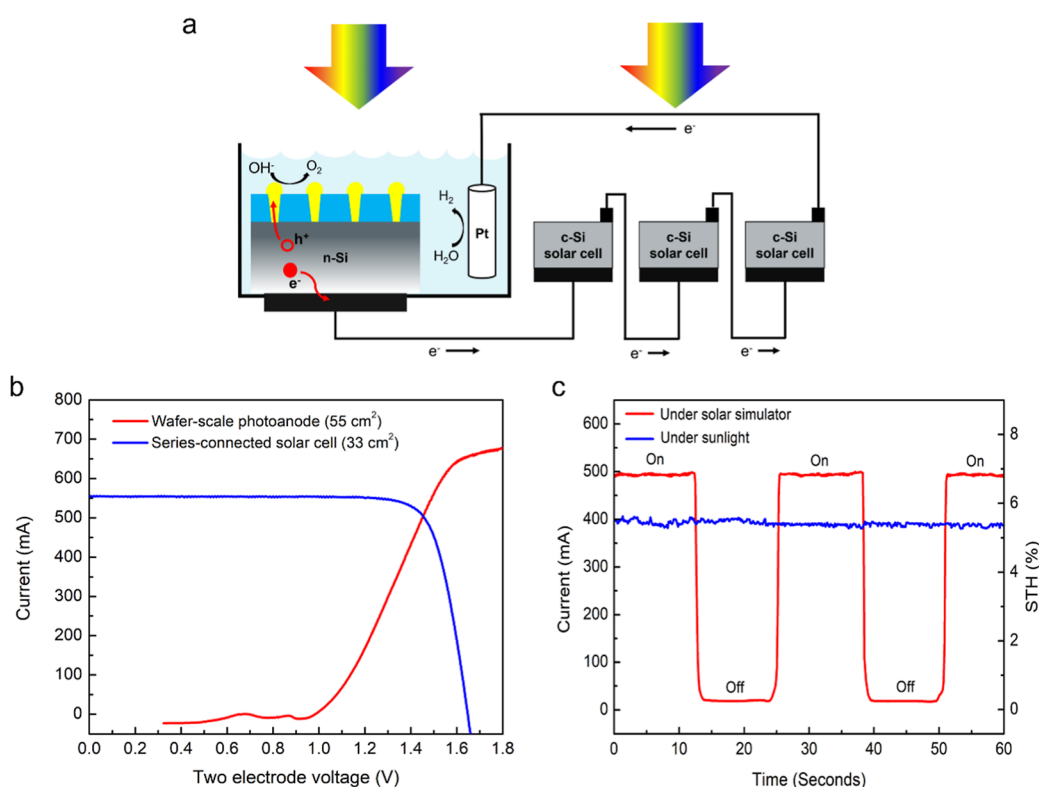
Figure 6. PEC performance of unassisted solar-driven water splitting system. (a) Schematics of unassisted water splitting system with wafer-scale photoanode and monocrystalline Si solar cells. (b) I−V curves of monocrystalline Si solar cell and wafer-scale photoanode in a two-electrode system under AM 1.5G illumination. (c) CA measurements of unassisted solar-driven water splitting system under AM 1.5G simulated solar illumination and real outdoor sunlight.

Figure 5c shows the PEC performance of spiked NiFe/Ni/SiO$_2$/Si photoanodes for different surface coverages of NiFe/Ni, obtained at different electrodeposition times. Before NiFe electrodeposition, all spiked Ni/SiO$_2$/Si photoanodes were prepared with the same Ni coverage of 22% on the surface. As shown in Figure 5c, the NiFe/Ni coverages on the surface were 39, 62, and 84% after NiFe electrodeposition at −3.0 V applied bias for 5, 10, and 15 min, respectively. The spiked NiFe/Ni/SiO$_2$/Si photoanode with 10 min of NiFe deposition (62% coverage) shows the best OER performance with the lowest onset potential and highest saturation current density. For 5 min NiFe deposition (39% coverage), the lower contact area between the NiFe catalyst and electrolyte in the aqueous solution leads to reduced OER performance. For the spiked NiFe/Ni/SiO$_2$/Si photoanode with 15 min NiFe deposition (84% coverage), the onset potential and fill factor similar to those for the photoanode with 10 min NiFe deposition (62% coverage) were observed. However, a reduced saturation photocurrent density (13 mA/cm^2) was also observed, since excessive NiFe coverage suppresses incident light absorption at the front side of the photoanode. The OER performance was also investigated by analysis with ABPE curves calculated from measured LSV curves and normalized to the peak value for optimum NiFe/Ni coverage. As shown in Figure 5d, the spiked NiFe/Ni/SiO$_2$/Si photoanode with 10 min of NiFe deposition (62% coverage) achieved the highest OER performance at 1.0 V versus RHE compared to other photoanodes with different NiFe/Ni coverages. We note that optimal NiFe coverage levels are likely to vary with illumination intensity due to the trade-off, with increased coverage, between increased catalytic

activity and reduced light transmission to the semiconductor absorber.

Wafer-Scale Photoanode Fabrication and PEC/PV Performance. For commercial H$_2$ production, large photoanode areas are required to increase the amount of evolved H$_2$ gas. The Al/SiO$_2$ thin film reaction and NiFe/Ni electrodeposition processes employed here are low-cost and highly scalable fabrication processes, the potential of which we demonstrate by fabricating a full wafer-scale spiked NiFe/Ni/SiO$_2$/Si photoanode on a 4 in. Si wafer. The wafer-scale photoanode was fabricated with a NiFe/Ni catalyst layer with ∼60% surface coverage and 4:1 NiFe ratio. As shown in Figure 6a, an unassisted water splitting system was designed by combining a wafer-scale photoanode with three monocrystalline Si solar cells, each with an area of 11 cm^2, connected in series with each other and with the photoanode. The wafer-scale photoanode and a Pt counter electrode were immersed in a 1 M KOH aqueous solution to form a two-electrode system incorporating the three series-connected monocrystalline Si solar cells. In Figure 6b, the wafer-scale photoanode (red curve) shows clear a clear OER performance with an onset potential of 0.98 V vs Pt and saturation photocurrent of 691.5 mA under AM 1.5G illumination from a large-area solar simulator. The series-connected monocrystalline Si solar cells with a total exposed area of 33 cm^2 generated a total photocurrent of 553.5 mA and an open-circuit potential (V_{OC}) of 1.65 V with a fill factor (FF) of 0.81, corresponding to a power-conversion efficiency of 22.4%. The intersection of the two I−V curves occurs at a photocurrent of 502.4 mA and a voltage of 1.46 V, which would correspond to a STH efficiency of approximately 7.0%. Although the Al/SiO$_2$ thin-film

reaction and electrodeposition for double-layered NiFe/Ni catalyst are scalable processes, it is challenging in a laboratory-scale system to control the uniformity of voids in the SiO_2 layer and NiFe/Ni coverage on the whole surface of a 4 in. wafer (see Figure S2 in the Supporting Information). In addition, a two-electrode system does not use a reference electrode so the potential of the counter electrode changes during the PEC measurements.[19] The unstable potential at the counter electrode leads to a degraded photocurrent density compared to that of a three-electrode system.

As shown in Figure 6c, the photocurrent and STH of a full water splitting system containing a wafer-scale spiked NiFe/Ni/SiO_2/Si photoanode and three series-connected mono-crystalline Si solar cells were measured under both AM 1.5G simulated solar illumination (red curve) and real outdoor sunlight (blue curve). The measured photocurrent was 480 mA under AM 1.5G simulated solar illumination, corresponding to a 6.9% STH efficiency. For the unassisted solar-driven water splitting system under real outdoor sunlight, a photocurrent of 396 mA and a 5.5% STH efficiency were obtained. Since illumination with real outdoor sunlight creates shadows on the wafer-scale photoanode, the resulting efficiency was lower compared to the measurement under the solar simulator. However, these results demonstrate the clear possibility of realizing a PEC H_2 production system using wafer-scale photoanodes combined with Si PV cells to provide the necessary additional bias voltage.

■ CONCLUSIONS

In summary, we have employed simple and highly scalable processes for the fabrication of high-performance Si-based MIS photoanodes incorporating localized conduction paths through thick SiO_2 insulating layers and double-layered NiFe/Ni catalysts. The localized conduction paths enable low-resistance charge extraction even through thick insulating layers, and this approach yields photoanodes with excellent stability. The double-layered NiFe/Ni catalyst was formed by a two-step electrodeposition process to create efficient OER catalysts. The NiFe/Ni catalyst structure increases the Schottky barrier height between Si and the metal catalyst, lowering the photoanode onset potential. A photoanode with 62% NiFe coverage and Ni/Fe = 4:1 yielded an onset potential of 0.8 V vs RHE and saturation current density over 25 mA/cm² under illumination with a 150 W unfiltered Xe lamp. In addition, a wafer-scale photoanode was fabricated using the same fabrication method on a 4-in. Si wafer, and the resulting photoanode was combined with three series-connected c-Si solar cells to create an unassisted solar-driven water splitting system. The fabricated water splitting system yielded 6.9% STH efficiency under simulated AM 1.5G sunlight illumination. These results demonstrate a readily adaptable approach for the design of PEC-based H_2 production systems.

■ EXPERIMENTAL SECTION

Fabrication of NiFe/Ni/SiO_2/n-Si Photoanodes with Localized Spike Structures. 4-in. n-type (100) c-Si wafers (thickness $t \sim$ 550 μm and resistivity ρ = 0.3–0.5 Ω cm) were cleaned using a standard piranha process. To remove the native oxide from the c-Si surface, cleaned substrates were immersed into a 5% HF aqueous solution for 1 min at room temperature. The front side of the Si wafer was then passivated by a high quality 90 nm SiO_2 layer that was thermally grown using an oxidation furnace (MRL 8′ furnace, Sandvik Thermal Process Inc.) at 1100 °C for 50 min in dry ambient O_2 ambient. To obtain the localized spiked structure on the SiO_2 layer, a

100 nm Al−Si film containing 1% Si was deposited onto the SiO_2/Si substrate via DC magnetron sputtering. Subsequently, the Al/SiO_2/Si substrate was annealed at 550 °C for 24 h in a vacuum chamber (V/IG 800 Series Vacuum/Inert Gas Oven). After formation of Al spikes in the Al/SiO_2/Si substrate via Al thin-film reaction, the Al−Si film was etched by dipping into 10% H_3PO_4 aqueous solution for 12 h and rinsed in DI water. The resulting spiked SiO_2/Si substrate was dried under a N_2 flow. A 300 nm Al layer was deposited on the rear surface of the wafer as a back contact by DC magnetron sputtering (UNIVEX 450B) under 1×10^{-6} Torr of base pressure. The spiked SiO_2/Si samples were then cleaved into 2×2 cm² samples. A Ni catalyst was first deposited on the exposed Si areas by electrodeposition. Subsequently, a NiFe layer was deposited on the resulting Ni islands by a second electrodeposition process. During the two-step electrodeposition, only the front side of the spiked SiO_2/Si substrate was exposed to the plating solution. A Pt counter electrode was dipped into the plating solution, and the working electrode was connected to the backside contact of the spiked SiO_2/Si substrate. The initial Ni electrodeposition was performed with a Ni plating solution consisting of 0.05 M $NiSO_4$, 0.05 M L-histidine, and 0.04 M boric acid aqueous solution. The Ni layers were deposited with an applied bias of −3.0 V for 5 min until covering the whole exposed Si surface on the spiked SiO_2/Si substrate. The NiFe plating solutions were made by adding different molar ratios of $FeSO_4$ (0.004–0.01 M) to a Ni plating solution consisting of 0.05 M $NiSO_4$, 0.05 M L-histidine, and 0.04 M boric acid aqueous solution. The sequential NiFe electrodeposition was performed at −3.0 V applied bias with deposition times ranging from 0 to 30 min.

Fabrication of Wafer-Scale NiFe/Ni/SiO_2/n-Si Photoanode. 4-in. wafer-scale spiked SiO_2/n-Si substrates with backside contacts were prepared using the same methods as described above. For electrodeposition, the wafer-scale substrate, large-scale container (750 mL), and counter electrode (100 nm Au/Ti film on 25×75 mm² slide glass) were prepared. Ni electrodeposition was performed with an applied bias of −3.0 V for 10 min using 500 mL Ni plating solution containing 0.05 M NiSO4, 0.05 M L-histidine, 0.04 M boric acid, 10% IPA aqueous solution. After the formation of uniform Ni islands, NiFe catalysts with 4:1 Ni/Fe ratio were deposited by electrodeposition with 500 mL NiFe plating solution (0.05 M NiSO4, 0.007 M FeSO4, 0.05 M L-histidine, 0.04 M boric acid, 10% IPA aqueous solution) under applied bias of −3.0 V for 40 min.

PEC Measurements and Analysis with Tafel Plot. All PEC measurements were carried out with a CHI 760E electrochemical workstation (CH Instruments, Austin, TX, United States) with a standard three-electrode electrochemical cell consisting of Pt wire as a counter electrode and a Ag/AgCl reference electrode. A 1 M KOH aqueous solution was prepared for the alkaline solution (pH = 14) for the OER characterization. The measured potentials were calibrated to RHE using eq 1

$$E_{RHE} = E_{Ag/AgCl} + 0.197V + 0.059 \times pH \qquad (1)$$

The LSV and CA measurements were carried out under 150 W light illumination using a Xenon arc lamp (66475, Newport) for characterization of photoanodes. The performance of the photoanode was evaluated by calculating the ABPE using eq 2.[46]

$$ABPE = \frac{P_{out} - P_{in}}{P_{light}} = \frac{J_{ph}(V_{redox} - V_{bias})}{P_{light}} \qquad (2)$$

where V_{redox} is the redox potential for water splitting, V_{bias} refers to the potential difference between the working and counter electrodes, P_{light} is the light power intensity, and J_{ph} is the measured photocurrent density. For the OER polarization measurement, the thick NiFe films were prepared by NiFe electrodeposition on Ni foil with different NiFe plating solutions under −5.0 V applied bias for 2 h. The OER characterization measurements were performed with a three-electrode system. The measured OER polarization curve was analyzed by calculating the Tafel slope using eq 3.[46]

$$\eta = \pm A \times \log_{10}\left(\frac{J}{J_0}\right) \tag{3}$$

where η is the overpotential, A is the Tafel slope, J is the current density, and J_0 is the exchange photocurrent density.

The unassisted water splitting system was constructed by connecting a wafer-scale photoanode and three commercial monocrystalline Si solar cells (Solar Made Corp.) in series. The performance of the unassisted water splitting system was measured under simulated AM 1.5G illumination (ABET Technologies, Sun 2000 Class A). The STH conversion efficiency is calculated using eq 4 assuming a Faradaic efficiency (η_F) of 100%.[47]

$$STH = \frac{\eta_F \times I_{OP} \times 1.23V}{P_{in} \times (A_{photoanode} + A_{solar\ cells})} \times 100\% \tag{4}$$

where I_{OP} is the operating current of the PV/PEC device, P_{in} is the input energy, $A_{photoanode}$ and $A_{solar\ cells}$ are area of wafer-scale photoanode (55 cm^2) and Si solar cells (33 cm^2), respectively.

Characterization. The surface morphologies of electrodeposited NiFe/Ni surfaces were carried out using field emission SEM (Zeiss Neon 40, USA). The elemental analysis was carried out using EDX spectroscopy (Bruker EDS) for SEM. The surface coverages of electrodeposited NiFe/Ni catalyst layers were calculated by using the "ImageJ" platform. The numerical simulations for spiked NiFe/SiO$_2$/Si and spiked Ni/SiO$_2$/Si structures were performed using the semiconductor module of a commercial numerical finite-element solver (COMSOL Multiphysics).

■ ASSOCIATED CONTENT

ⓈI Supporting Information

The Supporting Information is available free of charge at https://pubs.acs.org/doi/10.1021/acsaem.4c00016.

Plan-view SEM image of electrodeposited NiFe film on Ni plate; and photograph of wafer-scale (4-inch) spiked NiFe/Ni/SiO2/Si photoanode and corresponding SEM images of wafer-scale (4-inch) spiked NiFe/Ni/SiO2/Si photoanode in different regions (PDF)

■ AUTHOR INFORMATION

Corresponding Author

   Edward T. Yu − Microelectronics Research Center, Chandra Family Department of Electrical and Computer Engineering, The University of Texas at Austin, Austin, Texas 78758, United States; Email: ety@ece.utexas.edu

Authors

   Soonil Lee − Microelectronics Research Center, Chandra Family Department of Electrical and Computer Engineering, The University of Texas at Austin, Austin, Texas 78758, United States

   Shang-Hsuan Wu − Microelectronics Research Center, Chandra Family Department of Electrical and Computer Engineering, The University of Texas at Austin, Austin, Texas 78758, United States; Ⓞ orcid.org/0000-0001-9934-7765

Complete contact information is available at:
https://pubs.acs.org/10.1021/acsaem.4c00016

Author Contributions

[†]S.L. and S.-H.W contributed equally to this work.

Notes

The authors declare no competing financial interest.

■ REFERENCES

(1) Gao, R.-T.; Liu, L.; Li, Y.; Yang, Y.; He, J.; Liu, X.; Zhang, X.; Wang, L.; Wu, L. Ru-P pair sites boost charge transport in hematite photoanodes for exceeding 1% efficient solar water splitting. *Proc. Natl. Acad. Sci. U.S.A.* **2023**, *120* (27), No. e2300493120.

(2) Gao, R.-T.; Zhang, J.; Nakajima, T.; He, J.; Liu, X.; Zhang, X.; Wang, L.; Wu, L. Single-atomic-site platinum steers photogenerated charge carrier lifetime of hematite nanoflakes for photoelectrochemical water splitting. *Nat. Commun.* **2023**, *14* (1), 2640.

(3) Liu, B.; Wang, X.; Zhang, Y.; Xu, L.; Wang, T.; Xiao, X.; Wang, S.; Wang, L.; Huang, W. A BiVO4 Photoanode with a VOx Layer Bearing Oxygen Vacancies Offers Improved Charge Transfer and Oxygen Evolution Kinetics in Photoelectrochemical Water Splitting. *Angew. Chem., Int. Ed.* **2023**, *62* (10), No. e202217346.

(4) Gao, R.-T.; Nguyen, N. T.; Nakajima, T.; He, J.; Liu, X.; Zhang, X.; Wang, L.; Wu, L. Dynamic semiconductor-electrolyte interface for sustainable solar water splitting over 600 hours under neutral conditions. *Sci. Adv.* **2023**, *9* (1), No. eade4589.

(5) Kenney, M. J.; Gong, M.; Li, Y.; Wu, J. Z.; Feng, J.; Lanza, M.; Dai, H. High-Performance Silicon Photoanodes Passivated with Ultrathin Nickel Films for Water Oxidation. *Science* **2013**, *342* (6160), 836−840.

(6) Ji, L.; Hsu, H.-Y.; Li, X.; Huang, K.; Zhang, Y.; Lee, J. C.; Bard, A. J.; Yu, E. T. Localized dielectric breakdown and antireflection coating in metal-oxide-semiconductor photoelectrodes. *Nat. Mater.* **2017**, *16* (1), 127−131.

(7) Lee, S.; Ji, L.; De Palma, A. C.; Yu, E. T. Scalable, highly stable Si-based metal-insulator-semiconductor photoanodes for water oxidation fabricated using thin-film reactions and electrodeposition. *Nat. Commun.* **2021**, *12* (1), 3982.

(8) Mikolasek, M.; Frohlich, K.; Husekova, K.; Racko, J.; Rehacek, V.; Chymo, F.; Tapajna, M.; Harmatha, L. Silicon based MIS photoanode for water oxidation: A comparison of RuO2 and Ni Schottky contacts. *Appl. Surf. Sci.* **2018**, *461*, 48−53.

(9) Digdaya, I. A.; Trześniewski, B. J.; Adhyaksa, G. W. P.; Garnett, E. C.; Smith, W. A. General Considerations for Improving Photovoltage in Metal-Insulator-Semiconductor Photoanodes. *J. Phys. Chem. C* **2018**, *122* (10), 5462−5471.

(10) Cai, Q.; Hong, W.; Jian, C.; Li, J.; Liu, W. Insulator Layer Engineering toward Stable Si Photoanode for Efficient Water Oxidation. *ACS Catal.* **2018**, *8* (10), 9238−9244.

(11) Liu, B.; Feng, S.; Yang, L.; Li, C.; Luo, Z.; Wang, T.; Gong, J. Bifacial passivation of n-silicon metal-insulator-semiconductor photoelectrodes for efficient oxygen and hydrogen evolution reactions. *Energy Environ. Sci.* **2020**, *13* (1), 221−228.

(12) Chymo, F.; Fröhlich, K.; Kundrata, I.; Hušeková, K.; Harmatha, L.; Racko, J.; Breza, J.; Mikolášek, M. Characterization of MIS photoanode with a thin SiO2 layer for photoelectrochemical water splitting. *AIP Conf. Proc.* **2019**, *2131* (1), 020020.

(13) Law, M. E.; Solley, E.; Liang, M.; Burk, D. E. Self-consistent model of minority-carrier lifetime, diffusion length, and mobility. *IEEE Electron Device Lett.* **1991**, *12* (8), 401−403.

(14) Wieder, A. W. Emitter effects in shallow bipolar devices: Measurements and consequences. *IEEE Trans. Electron Devices* **1980**, 27 (8), 1402−1408.

(15) Zhao, Y.; Descamps, J.; Ababou-Girard, S.; Bergamini, J.-F.; Santinacci, L.; Léger, Y.; Sojic, N.; Loget, G. Metal-Insulator-Semiconductor Anodes for Ultrastable and Site-Selective Upconversion Photoinduced Electrochemiluminescence. *Angew. Chem., Int. Ed.* **2022**, 61, No. e202201865.

(16) Liu, Z.; Li, C.; Xiao, Y.; Wang, F.; Yu, Q.; Faheem, M. B.; Zhou, T.; Li, Y. Tailored NiFe Catalyst on Silicon Photoanode for Efficient Photoelectrochemical Water Oxidation. *J. Phys. Chem. C* **2020**, 124 (5), 2844−2850.

(17) Oh, K.; Dorcet, V.; Fabre, B.; Loget, G. Dissociating Water at n-Si Photoanodes Partially Covered with Fe Catalysts. *Adv. Energy Mater.* **2020**, 10 (3), 1902963.

(18) Zhong, D. K.; Sun, J.; Inumaru, H.; Gamelin, D. R. Solar Water Oxidation by Composite Catalyst/α-Fe2O3 Photoanodes. *J. Am. Chem. Soc.* **2009**, 131 (17), 6086−6087.

(19) Lee, S. A.; Lee, T. H.; Kim, C.; Lee, M. G.; Choi, M.-J.; Park, H.; Choi, S.; Oh, J.; Jang, H. W. Tailored NiO<i>x</i>/Ni Cocatalysts on Silicon for Highly Efficient Water Splitting Photoanodes via Pulsed Electrodeposition. *ACS Catal.* **2018**, 8 (8), 7261−7269.

(20) Pastor, E.; Le Formal, F.; Mayer, M. T.; Tilley, S. D.; Francàs, L.; Mesa, C. A.; Grätzel, M.; Durrant, J. R. Spectroelectrochemical analysis of the mechanism of (photo)electrochemical hydrogen evolution at a catalytic interface. *Nat. Commun.* **2017**, 8 (1), 14280.

(21) Jeon, T. H.; Kim, B.; Kim, C.; Xia, C.; Wang, H.; Alvarez, P. J. J.; Choi, W. Solar photoelectrochemical synthesis of electrolyte-free H2O2 aqueous solution without needing electrical bias and H2. *Energy Environ. Sci.* **2021**, 14 (5), 3110−3119.

(22) Suzuki, H.; Nitta, S.; Tomita, O.; Higashi, M.; Abe, R. Highly Dispersed RuO2 Hydrates Prepared via Simple Adsorption as Efficient Cocatalysts for Visible-Light-Driven Z-Scheme Water Splitting with an IO3-/I- Redox Mediator. *ACS Catal.* **2017**, 7 (7), 4336−4343.

(23) Li, J.-M.; Hu, C.-C.; Wu, T.-H.; Hsu, Y.-J. Electroless deposition of RuO2-based nanoparticles for energy conversion applications. *RSC Adv.* **2019**, 9 (8), 4239−4245.

(24) Li, L.; Yang, J.; Ali-Löytty, H.; Weng, T.-C.; Toma, F. M.; Sokaras, D.; Sharp, I. D.; Nilsson, A. Operando Observation of Chemical Transformations of Iridium Oxide During Photoelectrochemical Water Oxidation. *ACS Appl. Energy Mater.* **2019**, 2 (2), 1371−1379.

(25) Minguzzi, A.; Naldoni, A.; Lugaresi, O.; Achilli, E.; D'Acapito, F.; Malara, F.; Locatelli, C.; Vertova, A.; Rondinini, S.; Ghigna, P. Observation of charge transfer cascades in α-Fe2O3/IrOx photoanodes by operando X-ray absorption spectroscopy. *Phys. Chem. Chem. Phys.* **2017**, 19 (8), 5715−5720.

(26) Li, W.; Sheehan, S. W.; He, D.; He, Y.; Yao, X.; Grimm, R. L.; Brudvig, G. W.; Wang, D. Hematite-Based Solar Water Splitting in Acidic Solutions: Functionalization by Mono- and Multilayers of Iridium Oxygen-Evolution Catalysts. *Angew. Chem., Int. Ed.* **2015**, 54 (39), 11428−11432.

(27) Yu, X.; Yang, P.; Chen, S.; Zhang, M.; Shi, G. NiFe Alloy Protected Silicon Photoanode for Efficient Water Splitting. *Adv. Energy Mater.* **2017**, 7 (6), 1601805.

(28) She, H.; Yue, P.; Ma, X.; Huang, J.; Wang, L.; Wang, Q. Fabrication of BiVO4 photoanode cocatalyzed with NiCo-layered double hydroxide for enhanced photoactivity of water oxidation. *Appl. Catal., B* **2020**, 263, 118280.

(29) Bae, D.; Mei, B.; Frydendal, R.; Pedersen, T.; Seger, B.; Hansen, O.; Vesborg, P. C. K.; Chorkendorff, I. Back-Illuminated Si-Based Photoanode with Nickel Cobalt Oxide Catalytic Protection Layer. *ChemElectroChem* **2016**, 3 (10), 1546−1552.

(30) Zhao, B.; Feng, C.; Huang, X.; Ding, Y.; Bi, Y. Coupling NiCo catalysts with carbon quantum dots on hematite photoanodes for highly efficient oxygen evolution. *J. Mater. Chem. A* **2022**, 10 (6), 2813−2818.

(31) Esposito, D. V.; Levin, I.; Moffat, T. P.; Talin, A. A. H2 evolution at Si-based metal-insulator-semiconductor photoelectrodes enhanced by inversion channel charge collection and H spillover. *Nat. Mater.* **2013**, 12 (6), 562−568.

(32) Maity, N. P.; Maity, R.; Baishya, S. Voltage and oxide thickness dependent tunneling current density and tunnel resistivity model: Application to high-k material HfO2 based MOS devices. *Superlattices Microstruct.* **2017**, 111, 628−641.

(33) Shan, C. X.; Hou, X.; Choy, K.-L. Corrosion resistance of TiO2 films grown on stainless steel by atomic layer deposition. *Surf. Coat. Technol.* **2008**, 202 (11), 2399−2402.

(34) Zhou, X.; Liu, R.; Sun, K.; Papadantonakis, K. M.; Brunschwig, B. S.; Lewis, N. S. 570 mV photovoltage, stabilized n-Si/CoOx heterojunction photoanodes fabricated using atomic layer deposition. *Energy Environ. Sci.* **2016**, 9 (3), 892−897.

(35) Fan, R.; Cheng, S.; Huang, G.; Wang, Y.; Zhang, Y.; Vanka, S.; Botton, G. A.; Mi, Z.; Shen, M. Unassisted solar water splitting with 9.8% efficiency and over 100 h stability based on Si solar cells and photoelectrodes catalyzed by bifunctional Ni-Mo/Ni. *J. Mater. Chem. A* **2019**, 7 (5), 2200−2209.

(36) Corrigan, D. A. The Catalysis of the Oxygen Evolution Reaction by Iron Impurities in Thin Film Nickel Oxide Electrodes. *J. Electrochem. Soc.* **1987**, 134 (2), 377−384.

(37) Takane, D.; Souma, S.; Sato, T.; Takahashi, T.; Segawa, K.; Ando, Y. Work function of bulk-insulating topological insulator Bi2-xSbxTe3-ySey. *Appl. Phys. Lett.* **2016**, 109 (9), 091601.

(38) Michaelson, H. B. The work function of the elements and its periodicity. *J. Appl. Phys.* **1977**, 48 (11), 4729−4733.

(39) Çankaya, G.; Uçar, N. Schottky Barrier Height Dependence on the Metal Work Function for p-type Si Schottky Diodes. *Z. Naturforsch., A: Phys. Sci.* **2004**, 59 (11), 795−798.

(40) Scheuermann, A. G.; Lawrence, J. P.; Kemp, K. W.; Ito, T.; Walsh, A.; Chidsey, C. E. D.; Hurley, P. K.; McIntyre, P. C. Design principles for maximizing photovoltage in metal-oxide-protected water-splitting photoanodes. *Nat. Mater.* **2016**, 15 (1), 99−105.

(41) Laskowski, F. A. L.; Oener, S. Z.; Nellist, M. R.; Gordon, A. M.; Bain, D. C.; Fehrs, J. L.; Boettcher, S. W. Nanoscale semiconductor/ catalyst interfaces in photoelectrochemistry. *Nat. Mater.* **2020**, 19 (1), 69−76.

(42) Masaharu, K.; Atsuhiro, K.; Saraswat, K.; Wong, H. S. P.; Yoshio, N. Fermi-level depinning in metal/Ge Schottky junction and its application to metal source/drain Ge NMOSFET. *2008 Symposium on VLSI Technology*, 2008; pp 54−55.

(43) Ikarashi, N.; Masuzaki, K. Silicide formation process in ultra-thin Ni-silicide film for advanced semiconductor devices: mechanism of NiSi2 formation at low temperature. *J. Phys.: Conf. Ser.* **2011**, 326 (1), 012051.

(44) Zhu, Q. G.; Iwasaki, H.; Williams, E. D.; Park, R. L. Formation of iron silicide thin films. *J. Appl. Phys.* **1986**, 60 (7), 2629−2631.

(45) Kalantarifard, S.; Bikas, R.; Nandy, S.; Lis, T.; Chae, K. H.; Najafpour, M. M. Water Oxidation in the Presence of a Nickel Coordination Compound: Decomposition Products, Fe Impurity in the Electrolyte, and a Candidate as a Catalyst. *J. Phys. Chem. C* **2022**, 126 (23), 9753−9761.

(46) Jiang, C.; Moniz, S. J. A.; Wang, A.; Zhang, T.; Tang, J. Photoelectrochemical devices for solar water splitting - materials and challenges. *Chem. Soc. Rev.* **2017**, 46 (15), 4645−4660.

(47) Ding, C.; Qin, W.; Wang, N.; Liu, G.; Wang, Z.; Yan, P.; Shi, J.; Li, C. Solar-to-hydrogen efficiency exceeding 2.5% achieved for overall water splitting with an all earth-abundant dual-photoelectrode. *Phys. Chem. Chem. Phys.* **2014**, 16 (29), 15608−15614.